Class:	RPT
Doc. no.:	TOF-TER-RP-0002
Rev.:	1
Prepared by:	PD
Approved by:	RBO
Date:	2019-11-15

TERMA

ESA Contract No. 4000125430/18/NL/GLC/hh

Characterization of QCGA ToF Sensor for Navigation Cameras Final Report

Prepared:

Peter Davidsen

Systems Engineer

Approved:

Digitally signed by Robert Olesen
DN: c=DK, o=TERMA A/S // CVR:41881828, cn=Robert Olesen, serialNumber=CVR:41881828-RID:16324526
Date: 2019.11.15 13:30:13 +01'00'

Robert Olesen

Product Assurance Manager

Authorized:

Gert Caspersen

Project Manager

Record of Changes

ECO	Description	Rev	Date
	Released	1	2019-11-15

Contents

Figures

Tables

1 Introduction

1.1 Purpose

The purpose of this final report is to conclude on the radiation tests performed on the Fraunhofer IMS QVGA time-of-flight sensor. This included modifications of the performance simulator developed as part of the "*RdV and Docking 3D Camera technology Trade-off and breadboard Demonstration*" study, as well as the execution of a few simulations taking into account the EOL performance of the dark current measurements.

.

1.2 Scope

This document describes the major findings of the activity, including a summary of the document deliverables resulting from the project.

2 References

Ref.	Doc. No.	Title
[RD1]	ESA-TRP-TECSAA-SOW-010525	Characterization of QVGA ToF sensor for navigation cameras
[RD2]	-	QVGA Photo-Detector for Indirect ToF-Imaging, Fraunhofer IMS, Duisburg, Germany
[RD3]	ECSS-E-ST-10-12C	Methods for the calculation of radiation received and its effects, and a policy for design margins
[RD4]	ETAO-TAS-TN-151	RdV and Docking 3D Camera technology Trade-off and breadboard Demonstration, Requirements Analysis Document, 2012-11-09
[RD5]	TOF-TER-CCN-0001	Design Concept Report and Critical Areas, 2019-09-10
[RD6]	TOF-TER-CCN-0001	RdV and Docking 3D Camera technology Trade-off and breadboard Demonstration, Performance Analysis, 2013-09-01

3 Terms and definitions

Term	Definition
AD	Applicable Document
APS	Active Pixel Sensor
COTS	Commercial Off the Shelf
ECSS	European Cooperation for Space Standardization
ELDRS	Enhanced Low Dose Rate Sensitivity
ESA	European Space Agency
FR	Final Review

Term	Definition
IMS	Institute for Microelectronic circuits and Systems
LET	Linear Energy Transfer
QVGA	Quarter Video Graphics Array
RD	Reference Document
RDV	Rendez Vous
RMS	Root mean square
SEL	Single Event Latch Up
Si	Silicon
SNR	Signal to Noise Ratio
TOF	Time of Flight
TRR	Test Readiness Review

4 Background and Objective

4.1 Background

The activity RDV and Docking 3D camera technology trade-off and BB demonstration was concluded in 2017. A prototype camera was manufactured and performances were measured.

The follow-on activity originally anticipated was to engage for critical design activity and the manufacturing of an Engineering Model. However, important elements have yet to be de-risked before this could be engaged.

First of all, the original detector used in the prototype is not commercially available anymore. An improved version of this detector from Fraunhofer-IMS is now available. The performances of this detector – in particular without the filter that was present on the earlier version – need to be characterized.

Secondly, due to the limited expected volumes of use of such a camera, it is not deemed feasible to develop a detector specific to the space use. Therefore, this activity shall de-risk the use of the detector in a space environment, especially through execution of radiation tests. Based on the outcome of this “small study”, the feasibility of a subsequent engineering model activity is to be assessed.

4.2 Objectives of the Activity

The current activity had the objectives given below [RD1]:

- To assess the performance of the new detector with increased resolution.
- To organize a radiation campaign focusing on total dose, proton displacement damage and heavy ions, in order to determine the suitability of this detector for a 3D navigation camera.

5 Management Overview

5.1 Work Breakdown Structure

The work carried out in scope of the project was decomposed as follows:

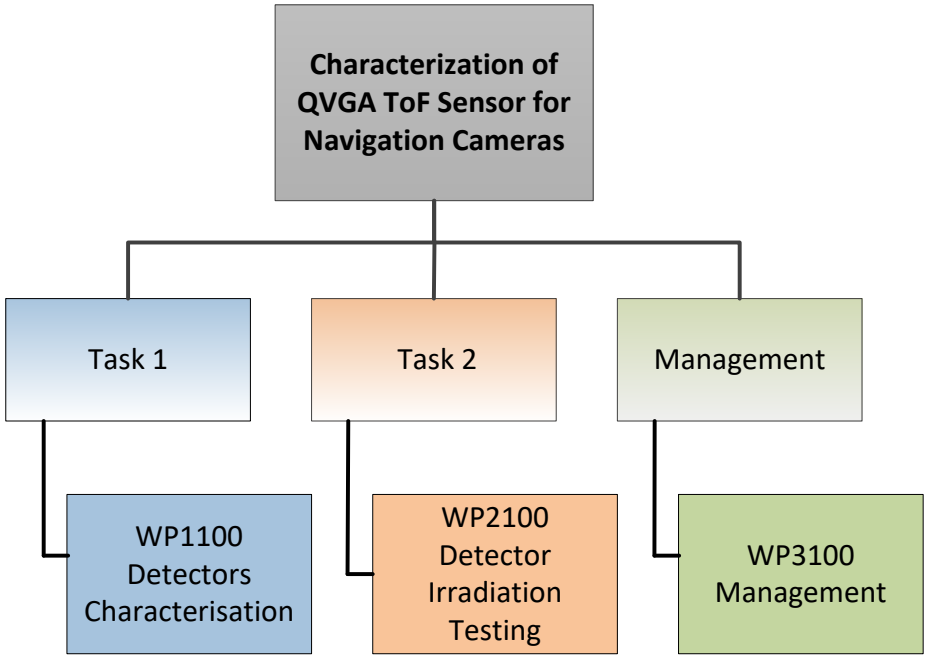

5.2 Work Package Description

The following work packages was conducted:

WP Name	Detectors Characterisation	**WP Number**	WP1100
Phase	Task 1: Detectors Characterisation		
WP Issue	1	**Date**	T0
Company	Terma A/S	**WP Manager**	Preben Bohn
Start Event	KO	**End Event**	TRR
Summary of Activities:	• As specified for Task 1 in the SoW		
WP Inputs	• Statement of Work. • 0005-0009073107, RDV and Docking 3D Camera Technology Tradeoff and Breadboard Demonstration Final Report		
WP Outputs	• Detector Radiation Test Plan – D1 • Detector Test Report – D2 (including preliminary characterisation before irradiation)		

WP Name	Detector Irradiation Testing	**WP Number**	WP2100
Phase	Task 2: Detector Irradiation Testing		
WP Issue	1	**Date**	T0+3 months
Company	Terma A/S	**WP Manager**	Peter Davidsen
Start Event	TRR	**End Event**	FR
Summary of Activities:	• As specified for Task 2 in the SoW		
WP Inputs	• Procured Detectors • Detector Radiation Test Plan – D1		
WP Outputs	• Detector Test Report – D2 (final version) • Recommendations for 3D Camera EM activity – D3		

WP Name	Management	**WP Number**	WP3100
Phase	Complete study		
WP Issue	1	**Date**	T0
Company	Terma A/S	**WP Manager**	Gert Caspersen
Start Event	KO	**End Event**	Project completion
Summary of Activities:	Perform overall management activities during the lifetime of the project. Responsible for the management and execution of the work to be performed. Activities includes: • Prepare review activities • Issue monthly status reports • Prepare and distribute Minutes of Meetings • Maintain documents and AI list • Maintain updated schedule		
WP Inputs	• Proposal • SOW		
WP Outputs	• Regular Progress Reports on activities • Minutes of Meetings • AI list, part of Progress Report • Schedule, part of Progress Report • Technical Data Packet		

6 Original Versus Actual Planning

Looking at the milestone plan, there has been a deviation between the dates scheduled at project kick-off – which took place on 31th October 2018 – and the actual execution dates as summarized in the following table:

Milestone	Scheduled Date	Actual Date
Test Readiness Review	2018-12-31	2018-12-07
Final Review	2019-06-31	2019-12-01

7 Radiation Test Objectives

7.1 Device under test

Fraunhofer IMS provided six QVGA image sensors in a PGA-132 ceramic package. Three of the six sensors were without the cover glass, but with a removable metal or ceramic lid. The three samples without cover glass were intended for testing with heavy ions. The remaining three ones were intended for proton testing.

7.2 Test Objective

The objective of the radiation tests was to assess the sensitivity of the device to radiation damage. Radiation can cause damage to the semiconductor that permanently degrades the electro-optical properties of the sensor or – since it is a CMOS device – cause a potential catastrophic latch up of the device making a camera based on this device inoperable. The two test objectives were therefore:

- Characterization of radiation induced degradation of electro-optical device parameters
- Measurement of the latch up immunity of the device, this is measurement of the LET threshold for susceptibility to latch up.

The electro-optical characterization of the sensors pre- and post-irradiation was performed by Fraunhofer IMS, Duisburg, Germany, and test procedures for the electro-optical tests are not part of this document.

8 Study Test Plan

8.1 Test Overview

As shown in Figure 1 below irradiation of the sensors took place after the initial electro-optical characterization of the samples. One half of the sensors was irradiated by protons, the other half was exposed to γ-radiation. After the irradiation was completed the sensors' electro-optical parameters were measured again and compared to the initial reference measurements.

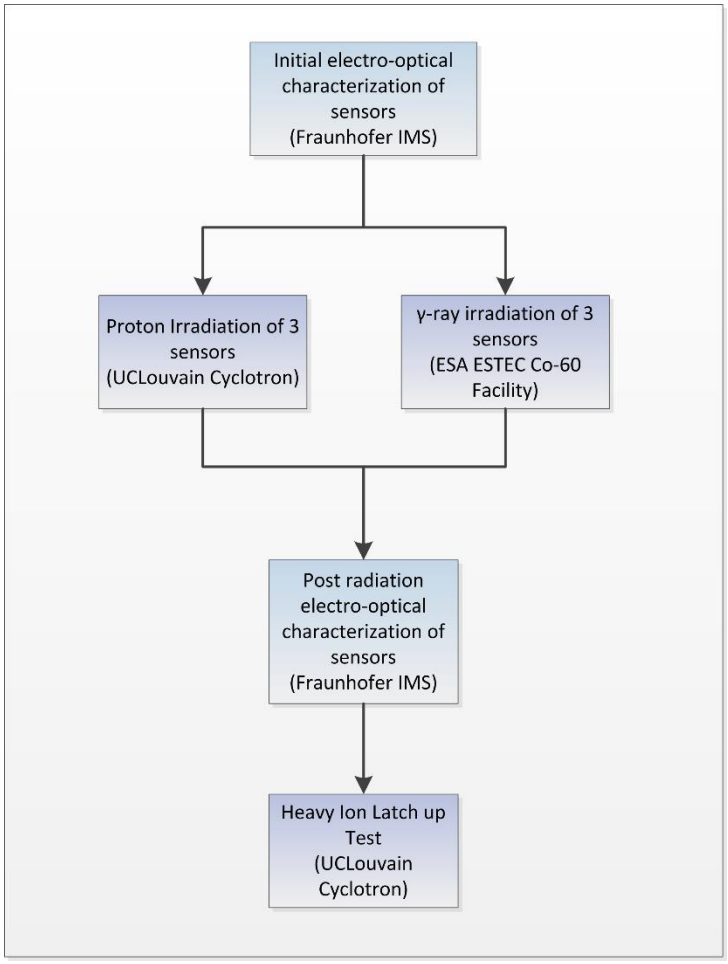

Figure 1 Test Flow Chart

Finally, heavy ion radiation was used to determine the single event latch up threshold of the device.

8.2 Proton Irradiation

8.2.1 Sample Preparation

The three QVGA sensors with glass cover from the previously electrically characterized sample lot were selected for proton irradiation.

Serial number/sample identifications were noted. Samples were mounted one at a time in the center of the target holder as shown in Figure 2. The devices were not powered during the irradiation.

Since the sensors were not mounted on a PCB, they were placed on a piece of conductive foam in order to avoid uncontrolled voltage build up on the device terminals.

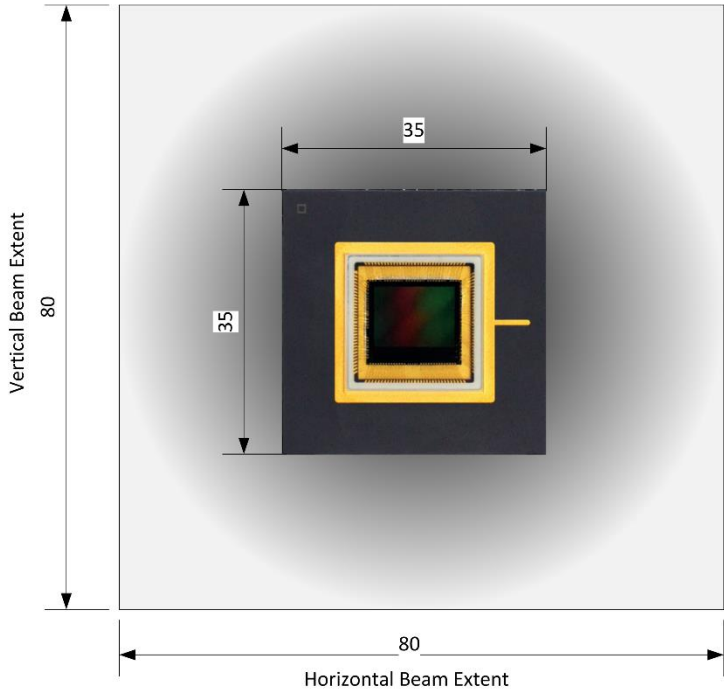

Figure 2 Sensor Placing in Beam Spot

There was no need for de-lidding of the samples, because proton attenuation through the cover glass is negligible. For example, energy loss for 60 MeV protons passing through boro-silicate glass is about 2.3 MeV/mm.

8.2.2 Test Facility / Beam Setup

The test facility used for the irradiation was the Light Ion Facility at the UCLouvain Cyclotron Resource Center.

The 65 MeV primary proton beam without degraders was used for the irradiation, resulting in an energy of 62 MeV at the sample position, which were reduced to about 60 MeV after passing through the cover glass.

8.2.3 Irradiation Procedure

The exposure levels for the three samples to be tested are listed in the table below

Sample Number	Targeted Exposure Level (protons/cm^2)
1	$1 \cdot 10^9$
2	$5 \cdot 10^9$
3	$10 \cdot 10^9$

Table 1 Exposure levels for proton irradiation

The maximum proton flux at the UCLouvain Light Ion Facility is $2 \cdot 10^8$ protons/(cm^2 s), which would result in rather short exposure times for the lowest test level. Depending on the

capabilities of the facility a flux in the order of $5 \cdot 10^7$ protons/(cm^2 s) corresponding to exposure times of 20, 100 and 200 seconds respectively.

Beam parameters like energy and flux and exposure times were protocolled in detail including an assessment of measurement uncertainties.

Control dosimetry of the proton beam was assumed to be carried out with equipment and procedures provided by the test facility.

8.3 γ-Radiation Irradiation

8.3.1 Sample Preparation

The three samples without cover glass were used for γ-irradiation. The protective metal/ceramic lid was removed for the irradiation. Serial numbers/sample identifications were noted. One sample at a time was mounted on the provided test board – see Figure 3.

The uniform irradiation area at the minimum distance to the ^{60}Co-source was about 16x16 cm^2, thus care was be taken to align the sample properly within the radiation area.

The samples were powered during the test. Five supply voltage with common ground were required 0.1, 2.8, 3,3, 5.0 and 8.0 V.

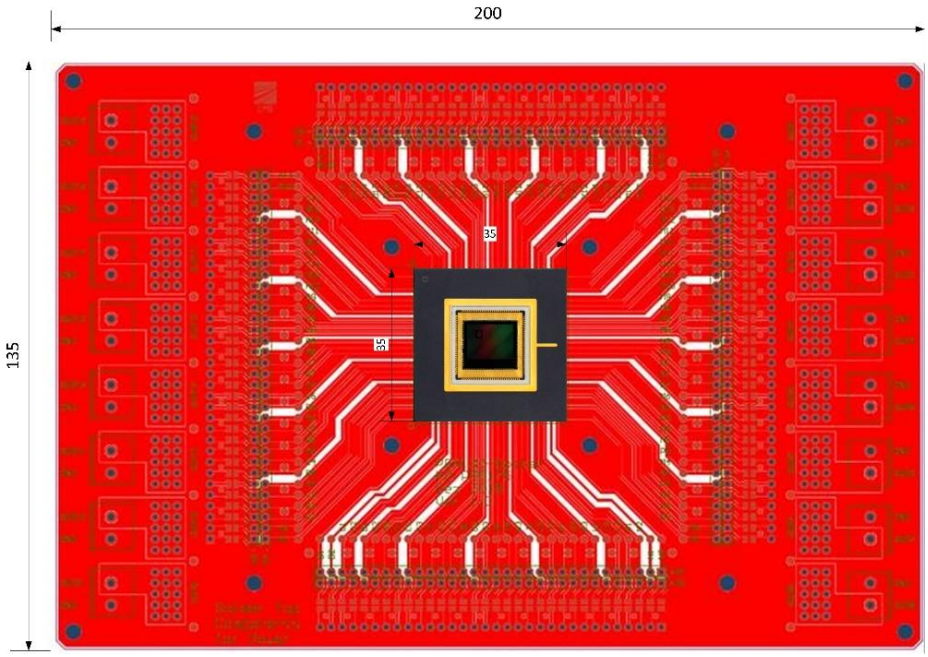

Figure 3 Sensors placed on the test PCB socket

8.3.2 Test Facility

The test facility used for the γ-irradiation of the sensors was the ESA-ESTEC Cobalt 60 facility. Depending on the distance from the source, the dose rate lies in the range of about 8.4 krad(Si)/h @ 40 cm and 23 rad(Si)/h @ 8 m[1].

8.3.3 Irradiation Procedure

The samples should receive a total dose according to Table 2

[1] Calculated with Dose Rate Calculator https://escies.org/webdocument/showArticle?id=262&groupid=6 and a rad(Water) to rad(Si) conversion factor of 0.895 for a photon energy of 1.17 MeV.

Sample Number	Targeted Dose Level (protons/cm^2)
1	1 krad(Si)
2	5 krad(Si)
3	10 krad(Si)

Table 2 Total γ-dose for the three samples

Since the sensors were CMOS devices, it was assumed that there were no ELDRS-related effects to consider. Also, the uniform irradiation area even at the shortest distance to the source was large to enough to cover all three sensors (Figure 3). Therefore, the sensors were placed at the smallest distance to the source that is practical possible at the day of the test in order to keep testing time short.

Exposure times for each sample were logged. Control dosimetry was provided by the test facility according to the test facilities' procedures.

8.4 Heavy Ion Testing

8.4.1 Sample Preparation / Test Setup

The three QVGA samples without cover glass previously used for γ-ray testing were used for this test.

The samples were one at a time inserted into the test PCB. Power was supplied to the test PCB from an external current limited supply that also counted latch up events on any of the five provided supply voltages (0.1, 2.8, 3.3, 5.0 and 8.0 V). The combined power supply/latch up counter was provided by Terma as an external unit (mains powered). The sensor under test was not clocked, read out, read in, or in any other way actively controlled during the test.

The current limiter output, which was the supply voltage of the device under test, was monitored by a counter circuit that was set to trigger on a voltage drop, indicating that a latch up had occurred. Once the event was counted, a reset pulse was generated that removed all device supply voltages for a predefined time of about 100 ms in order to clear the latch up condition. Counter dead time – to prevent false latch-up events while supply voltages stabilize – was about 1 s.

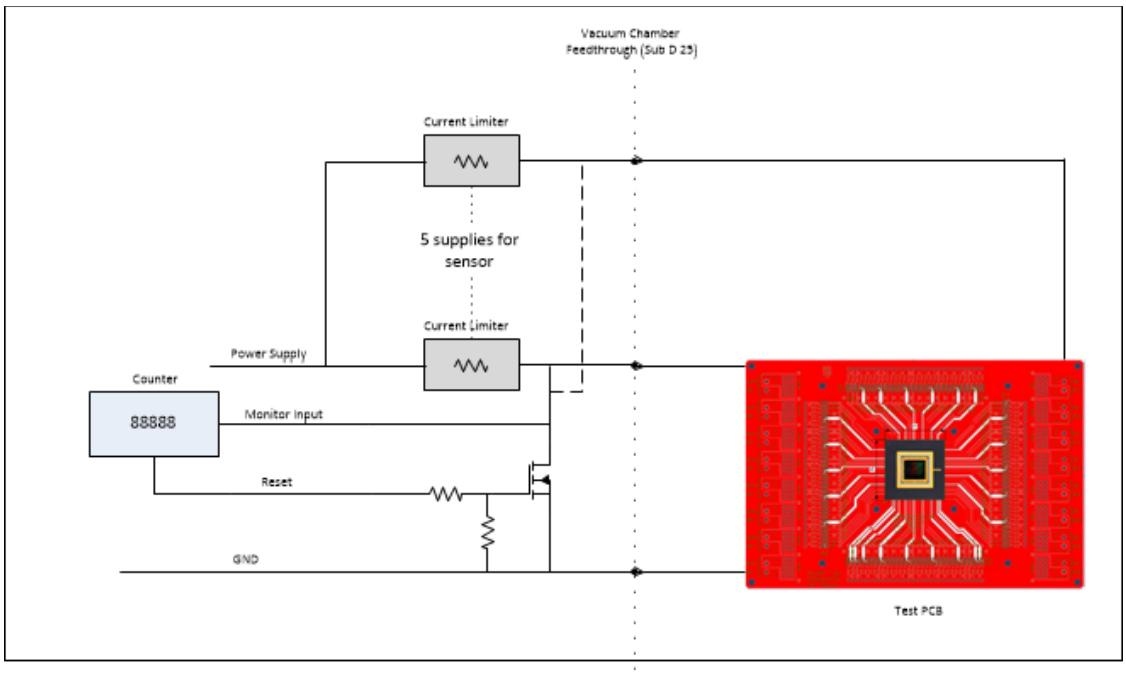

Figure 4 Test Circuit for Heavy Ion Testing

The homogeneous beam spot had a diameter of 25 mm, which was just enough to cover the sensor die (Figure 5). This meant only one sensor at a time could be inserted in the vacuum chamber. Furthermore, it was important to properly center the device relative to the beam center.

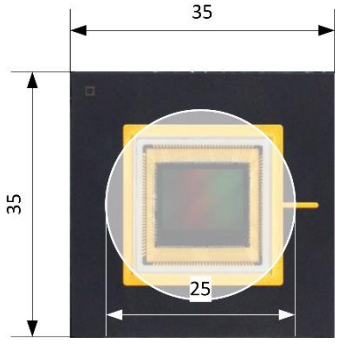

Figure 5 Beam spot on sensor

To ensure proper centering of the device to the beam, it was proposed to manufacture an aluminum support plate which could be screw-mounted on the UCLouvain Heavy Ion Support Frame. This aluminum support plate was equipped with fasteners for the test PCB, positioned in a way to ensure automatic centering of the device under test (see Figure 6).

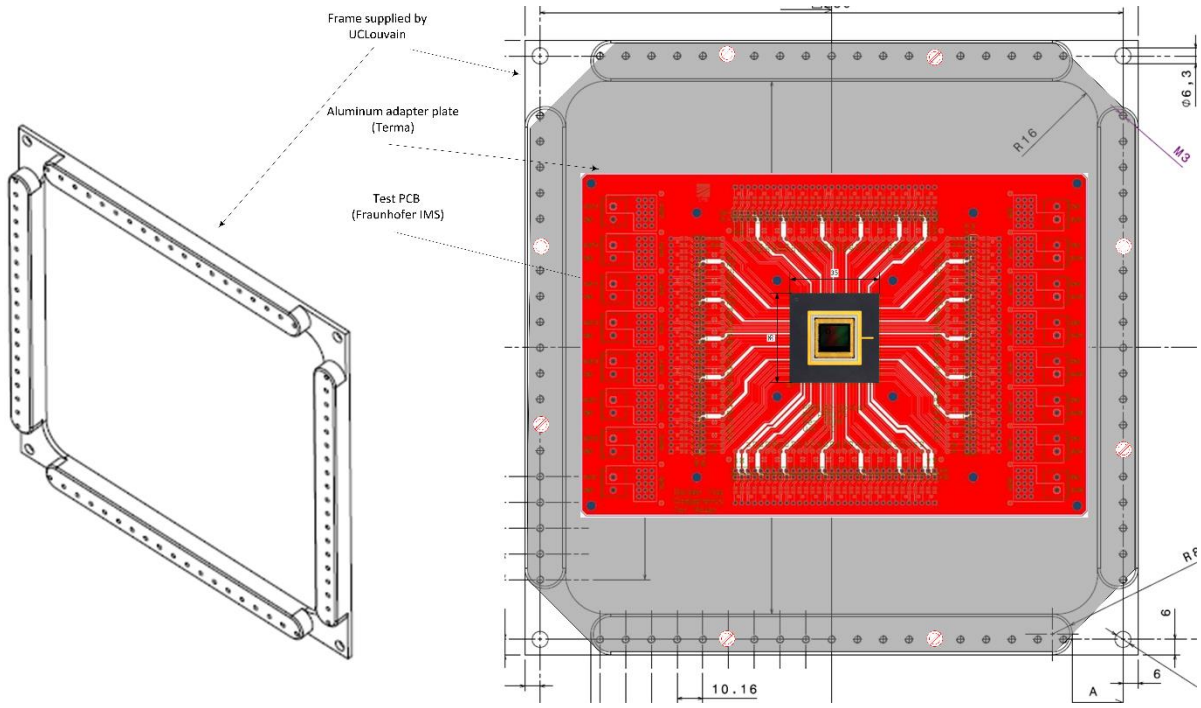

Figure 6 UCLouvain Heavy Ion Facility Sample Frame

8.4.2 Test Facility

The test was conducted at the heavy ion facility of the UCLouvain cyclotron. The beam cocktail contained ion species with a LET ranging from 1.3 to 62.5 MeV cm^2/mg in 9 steps, being sufficient to determine the LET dependent SEL cross-section of the device, if this proved to be necessary.

The maximum beam flux was $1.5 \cdot 10^4\ s^{-1}cm^{-2}$.

8.4.3 Irradiation Procedure

Test procedures for SEL testing differed, taking into account whether the devices were SEL sensitive or not. Therefore, an initial test where one device is irradiated with a high LET beam was conducted. Depending on the outcome of the initial test, further testing was made to either verify the non-sensitivity or to measure the SEL cross section of the devices as shown in Figure 7.

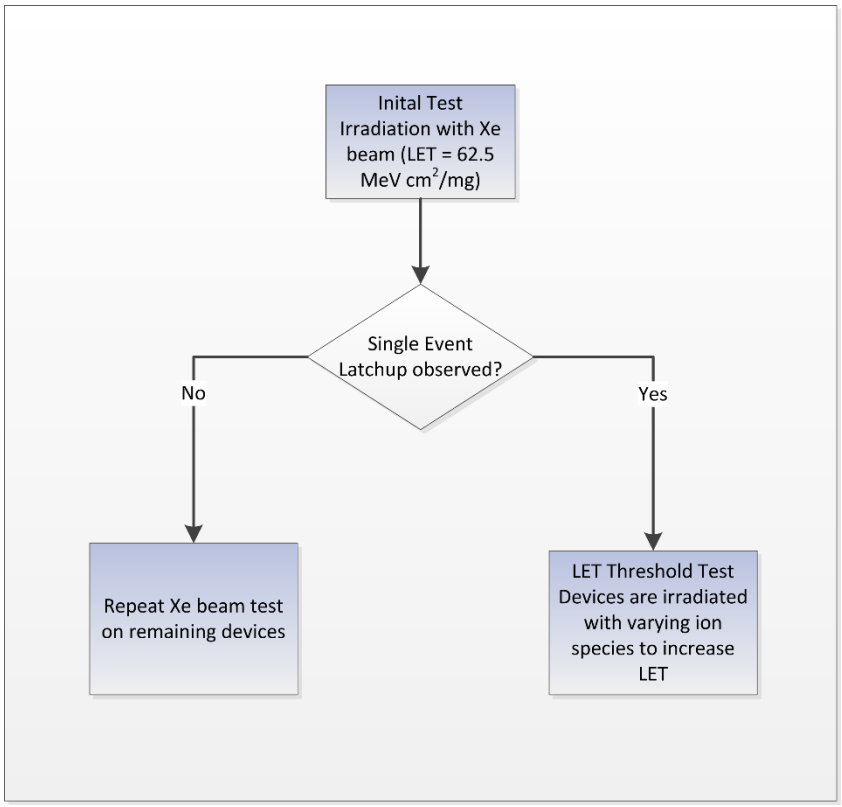

Figure 7 Latch up Testing Flow Chart

Beam flux was verified by beam intensity measurements provided by the UCLouvain Cyclotron facility. Exposure times and number of single events were logged for each test conducted. For cross-section calculation, the exposure time had to be corrected by the test circuits dead-time, being the time it takes to clear a latch up.

8.4.3.1 Initial Test

In order to find out whether the device is SEL sensitive, one device was irradiated with a $^{124}Xe^{35+}$ beam at maximum flux with the beam normal to the device.

Die size of the device was 1.44 cm^2 [RD2], which is completely covered by the incident beam (Figure 5) and assumed to be uniform over the irradiation area. SEL cross section is therefore given by the ratio of the number N of observed latch ups divided by the received fluence F:

$$\sigma_{SEL} = \frac{N}{F} = \frac{N}{\Phi\, t}$$

Irradiation time for a maximum upper bound of $\sigma_{SEL,max}$ is thus calculated by

$$t_{min} = \frac{1}{\Phi\, \sigma_{SEL,max}}$$

Setting the maximum cross section to σ_{SEL}= $1 \cdot 10^{-7}$ cm^2, this is reached after an irradiation for 667 s with the maximum flux Φ of $1.5 \cdot 10^4$ $s^{-1}cm^{-2}$.

In other words: If the device had not shown a latch up after 667 s, the device was regarded to be SEL latch up free according to clause 9.4.1.4.b [RD3]. In this case, testing continued with the procedures described in section 8.4.3.2. If a latch up occurred during irradiation with

the Xe-beam, the SEL cross section of the detector was measured according to the procedure outlined in section 8.4.3.3.

8.4.3.2 Verification of latch up immunity

In case no latch up was recorded during the initial test, the other two detectors were tested under the same conditions as described in the previous section. If latch up occurs during these tests, the initial assumption of insensitivity to SEL does not hold, and testing continues with measurement of the cross section as described in section 8.3.3.

8.4.3.3 Measurement of SEL cross section

The optimum strategy for measurement of the devices' SEL cross-section depends very much on how sensitive the devices are. If the device latches virtually immediately once exposed to the Xe-beam during initial testing, it can be assumed that the LET threshold is rather low. In this case it is best to start with low LET beams and increase LET by changing the ion species. If the devices are very sensitive to SEL, it is also advantageous to use the initial Xe-beam irradiation setup to find a reduced beam flux level that reduces the upset rate to less than 0.5 Hz ensuring that latch up events are not overlapping each other.

On the other hand, if the device shows only very few latch ups during the initial test, it is better to continue with high LET beams and reduce them subsequently. In this case testing continues with the maximum beam flux.

Irradiation time depends on the required measurement precision. Assuming that a statistical cross-section measurement error in the order of 20% is sufficient in the context of this study, 30 events have to be measured for each LET.

9 Radiation Tests Summary

A summary of the proton and total dose tests can be found in Table 3 below (*NSC: No Significant Change*). In essence, only the dark current (and non-uniformity) was affected by radiation as expected.

Parameter	1 krad	10 krad (biased)	10 krad (unbiased)	1e9 Protons	5e9 Proton	1e10 Proton
Dark Current	* 4	* 8.7	* 9.3	* 1.2	* 1.9	* 2.4
Temporal Dark Noise	NSC	* 1.5	* 2.5	NSC	* 0.5	NSC
Conversion Gain	NSC	NSC	NSC	NSC	NSC	NSC
Responsivity @ 528 nm	NSC	NSC	NSC	NSC	NSC	NSC
Responsivity @ 630 nm	NSC	NSC	NSC	NSC	NSC	NSC
Responsivity @ 850 nm	NSC	NSC	NSC	NSC	NSC	NSC
Quantum Efficiency @ 528 nm	NSC	NSC	NSC	NSC	NSC	NSC
Quantum Efficiency @ 630 nm	NSC	NSC	NSC	NSC	NSC	NSC
Quantum Efficiency @ 850 nm	NSC	NSC	NSC	NSC	NSC	NSC
Linearity Error	NSC	NSC	NSC	NSC	NSC	NSC
Sensitivity Threshold	NSC	* 1.5	* 2.5	NSC	* 0.5	NSC
Saturation Capacity	NSC	NSC	NSC	NSC	NSC	NSC
Sense Node Capacitance	NSC	NSC	NSC	NSC	NSC	NSC
Maximum SNR	NSC	NSC	NSC	NSC	NSC	NSC
Dynamic Range	NSC	NSC	NSC	NSC	NSC	NSC
DSNU	NSC	* 1.7	* 1.7	NSC	NSC	NSC
PRNU	NSC	* 2.7	* 1.5	NSC	* 0.5	NSC

Table 3: Radiation test summary

Marc Poizat, Radiation Effects Engineer (TEC-QEC - ESA/ESTEC) has kindly provided the following summary of the heavy ion test:

UCL - HIF. 08052019.									
Device number	Ion	LET (MeV.cm2/mg)	Average flux (cm-2/s)	Run duration (s)	Fluence (cm-2)	SEL number	Cross section (cm-2)	Run dose (krad)	Cumulated dose (krad)
69	Xe	62.5	1.50E+04	265	3.98E+06	311	7.81E-05	3.98E+00	3.98E+00
69	Rh	46.1	1.50E+04	255	3.83E+06	298	7.78E-05	2.83E+00	6.81E+00
69	Ni	20.4	1.66E+04	302	5.00E+06	90	1.80E-05	1.63E+00	8.44E+00
69	Ar	9.9	1.59E+04	630	1.00E+07	0	0.00E+00	1.58E+00	1.00E+01
69	Cr	16.1	1.59E+04	628	1.00E+07	83	8.30E-06	2.576	1.26E+01
69	Kr	32.4	1.58E+04	317	5.00E+06	333	6.66E-05	2.592	1.52E+01
59	Kr	32.4	1.56E+04	320	5.00E+06	346	0.0000692	2.592	2.592
59	Ar	9.9	1.55E+04	647	1.00E+07	0	0	1.584	4.176
59	Cr	16.1	1.52E+04	328	5.00E+06	54	0.0000108	1.288	5.464
61	Cr	16.1	1.59E+04	314	5.00E+06	44	0.0000088	1.288	1.288
61	Ar	9.9	16000	625	1.00E+07	0	0	1.584	2.872
61	Xe	62.5	15625	256	4.00E+06	299	0.00007475	4	6.872

Table 4: Heavy ion test data summary

The data has been fitted to the Weibull equation:

$$f(x) = A\left(1 - e^{-\left(\frac{x-x0}{W}\right)^{s}}\right)$$

A: $Limiting\ cross-section$
$x0$: SEE threshold
W: Weibull fit parameter
s: dimensionless Weibull fit exponent

With the results (see also Figure 8 on the next page):

A: $0.00008\ cm^2$
$x0$: $15\ \mathrm{MeV}cm^2/\mathrm{mg}$
W: $11.2\ \mathrm{MeV}cm^2/\mathrm{mg}$
s: 1.0

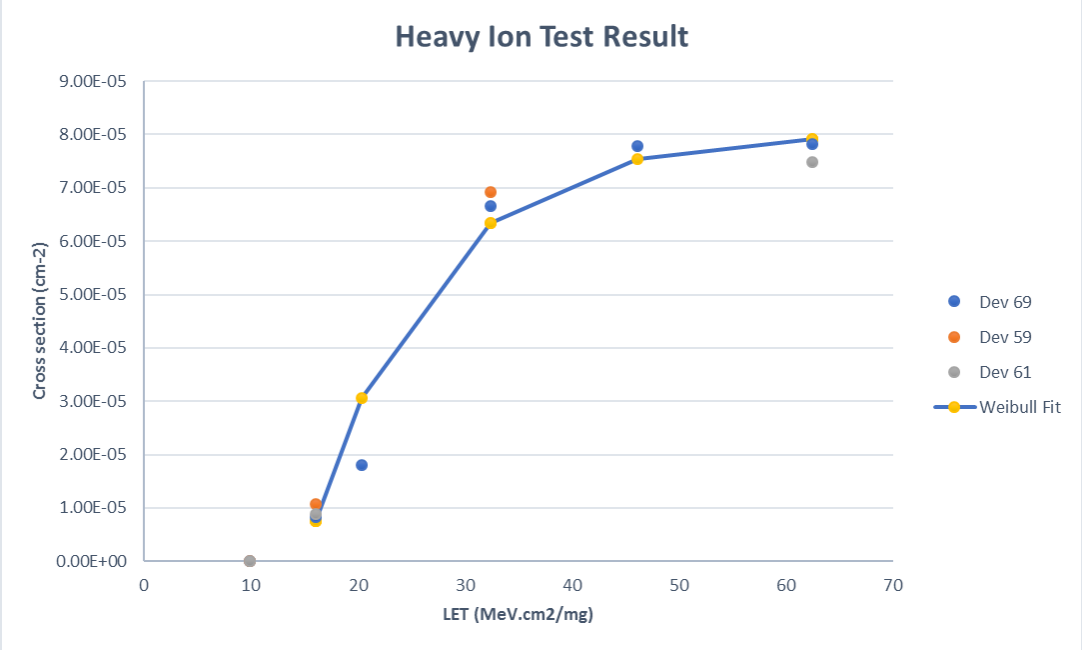

Figure 8: Heavy ion test results with fit for the QVGA ToF sensor

The detector is clearly not latch-up free. However, the LET threshold of approx. 15 MeVcm2/mg indicates that the device is statistically unlikely to be sensitive to proton induced SEL.

As such, a latch-up protection circuit must be included in the detector supply voltages.

10 Performance Analysis

In this section a performance analysis of the baseline ToF camera setup as described in [RD6] is presented. This performance model considers the following modifications, based on the initial breadboarding activities presented during the study "*RdV and Docking 3D Camera technology Trade-off and breadboard Demonstration, Requirements Analysis Document, 2012-11-09*", as well as testing of the new QVGA sensor:

1. The quantum efficiency of the ToF sensor used during the breadboarding activity – as specified by the datasheet – was too high compared to what was measured during the study activity. The reason for this was that the quantum efficiency was specified for the entire pixel and not just for each sub-pixel separately as used in the processing. In the test report for the new QVGA sensor, the QE is specified for each sub-pixel, which makes more sense from the point of view of a ToF application.
2. The optical laser output has been decreased in order to obtain more realistic estimates due to the following reasons:
    a. During the study it was found that even though the used PLDs were specified to be able to deliver 200+ watts, it was impossible to run them at this power output for long without damaging them. Better cooling would definitely help this. However, it should also be considered that the lifetime of the PLDs decreases fast with higher optical power output. As such the PLD optical power output has been decreased to a conservative 150W per PLD. Note that this is pulsed power obtained for a duty-cycle of less than 0.1%.

b. During the study, the PLD optics was briefly assessed. In the performance analysis it was however ignored, giving a best-case scenario performance assuming that all optical power was delivered in-field with zero variability. For more realistic measures, the optical power has been reduced by conservative 50% in order to take into account out-of-field spread as well as in-field variations in the following estimates.

3. The third sub-pixel – used in the initial performance analysis to eliminate background illumination by analog subtraction – is not available on the tested QVGA ToF sensor. This means that the full-well capacity alone determines the amount of background illumination the sensor can handle, but at the same time the noise will decrease. The auto-saturation time for the QVGA ToF sensor is ~20 seconds BOL and estimated to be ~2 seconds EOL.

10.1 Baseline Camera Parameters

The baseline camera setup consists of elements with the properties as described in Table 5 below (only a subset of all parameters is shown). See [RD6] for a full description of performance model and symbol definitions.

Symbol	Value	Comment
$b_{straylight}$	0 γ/px/s	Straylight amount. No (additional) straylight is assumed in baseline scenario. Please note that the baseline scenario includes Sun directly behind sensor, so the target itself will reflect a rather large amount of sunlight.
$d_{aperture}$	6 mm	Optical aperture. See [RD5]. Reduced from original assessment in order to improve depth of field.
DC	5000 e^-/px/s @ 20°C (BOL), 50000 e^-/px/s @ 20°C after 10 krad (EOL), 5K doubling temperature	Dark current. Test data for QVGA ToF sensor indicates ~5000 e^-/px/s pre-radiation and ~50000 e^-/px/s after 10 krad. The dark current is assumed to be doubled every 5 K. Note that this is significantly worse than the assumptions prior to the study. It will however be shown below that in-orbit estimation of dark current can significantly decrease the amount of error in the absolute range estimates.
FoV_{optics}	30° (diagonal)	Corresponding to 21.2° horizontal/vertical FoV for a square sensor. [RD4] requirement is 5-30°.
FoV_{laser}	21.2° (diagonal)	Set to be the inscribed circle of the sensor square, thus not wasting optical power outside the sensor field. This limits the amount of light hitting the sensor corners but for practical laser optics some light will always be emitted to the corners as well.
r	Variable	Range varies in simulation.
P_{laser}	10x150 W	Corresponding to 10 high power pulsed laser diodes from Laser Components, 905D3S3J08X. At 10 kHz and 100 ns

Symbol	Value	Comment
		pulse width, this corresponds to an average required electrical power of ~7 W for the diodes alone. [RD4] goal is 50W for the entire sensor. Note that a flat far-field emission pattern is not assumed; instead the optical power is intentionally decreased by 50% in the simulation to take into account out-of-field illumination and in-field variation. Note that the PLDs are specified to be able to handle up to +200 W pulsed power, but the power has been reduced in order to improve longevity.
R_{target}	0.3	Target reflectivity.
t_{pw}	100 ns	Maximum PLD pulse time for 0.1% duty cycle.
$\sigma_{readout}$	50 e^-	Readout noise. Terma star tracker experience.
θ	0	Only on-axis simulations used in this performance analysis. Off-axis angles are implemented in the model.
Δ_λ	20 nm	Filter bandwidth. Input from [RD5].
QE x FF	13.5% @ 630 nm	Quantum efficiency multiplied by fill-factor. From QVGA ToF sensor test results and specification.
Full-well capacity	148000 e^-	Approximately twice the amount as for the breadboard.

Table 5: Baseline time-of-flight camera parameters

In the following the performance of the baseline sensor setup is investigated.

10.2 Baseline Simulation

The models described in [RD6] were used to simulate a baseline sensor setup as described in section 10.1 above. For each range, 500 Monte Carlo simulations were performed to collect statistics on the sensor performance.

The controller electronics simulator was created in such a way that

- The two main triggers (i.e. not background trigger) are placed according to “expected” (i.e. simulated) range such that half of the returned pulse is located in the first trigger and the other half in the second trigger, if possible.
- The integration time of each trigger is set to the laser pulse width
- The number of accumulations is set dynamically prior to simulations by adjusting the number of accumulations until 50% of the maximum sensor readout is obtained. The maximum number of accumulations is however set so that the minimum frame rate is 10 Hz.
- No “search & acquisition” (S&A) phase is implemented in the simulator. In the simulator, the expected range – determining the trigger times – is simply set to the simulated range with half the pulse width added in random. In a real sensor – for ranges larger than half the chip-length of the laser pulse – a S&A is required: If – for

example – a chip length of 100 ns (30 m) is used for both laser and sensor, and the trigger start time is 0, a S&A phase is required to setup start trigger times if the target is more than 15 m away.

- Two different kinds of invalid measurements are identified:
    - If a measurement is below the expected readout noise, this – in general – means that no significant amount of light reached the sensor and the sensor value is declared invalid, shown by a sharp drop in the measurement accuracy. This can easily be implemented in the sensor CPU but there are a number of scenarios where it may not give robust results
    - If the absolute RMS error of the measurements is more than half the laser pulse width (in meters), the measurement is also marked as invalid. In principle, the measurements can actually still be used in a statistical sense. However, in a real sensor implementation, a tracker will need to constantly estimate the start trigger, and if the noise on the measurements exceeds half the laser pulse width it will be impossible for the tracker to estimate the trigger time correctly. For a 100 ns pulse-width, this corresponds to losing track at a 15 m error point, corresponding to 1% error at 1500 m range.

The performance simulator was modified to account for the new QVGA sensor. This meant changing the dark current methodology from being analog subtraction to DC-map dependent. This improved the DC noise, but lowered the saturation limit, which may cause saturation for highly reflective materials in direct sunlight. Note that for all simulations, the Sun is assumed to be directly behind the camera hitting the target at boresight, thus reflecting directly (although diffusively) into the camera. Specular reflections have not been considered.

It should be noted that calibration of light source characteristics (pulse shape and timing) and aging of components characteristics is not included in the performance model. As described in [RD5] some pre-flight and in-flight calibration methodologies are available to remedy this, but some impact on the final range estimate should be expected as none of the calibration options are perfect.

Additionally, the initial findings by SINTEF during calibration of the breadboard low-resolution sensor – showing that ToF measurements can be meaningless at horizontal high-intensity boundaries – have been ignored, as this issue will be minimized using a higher resolution sensor as well as using the technique for reconstruction of the depth-of-field employing the ToF estimates as described in [RD5].

Initially, the new simulator was tested without a dark current map estimator. The range error for the baseline sensor simulation without DC estimation is shown in Figure 9:

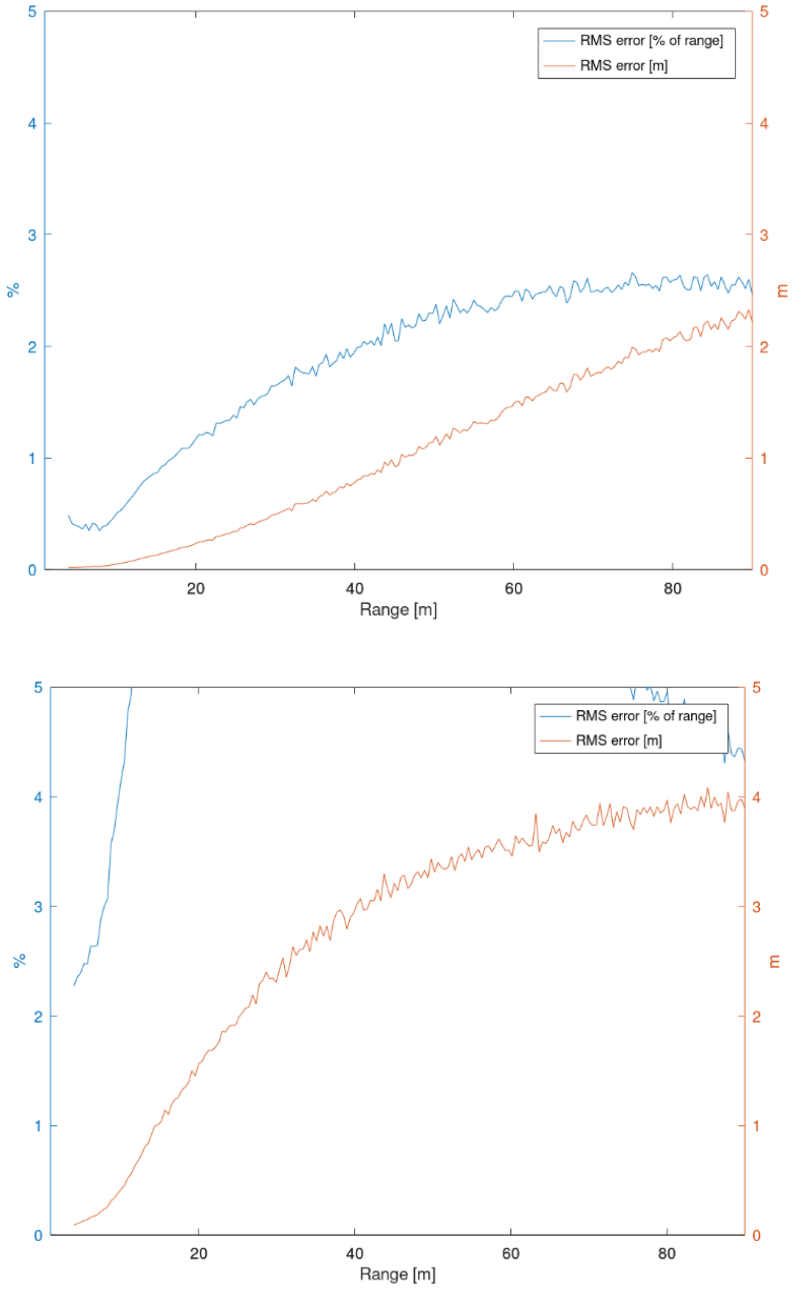

Figure 9: Baseline camera range performance BOL and EOL without DC estimation

Due to the large increase in DC at EOL, the range error increases dramatically. Further inspection of the sensor values shows that the problem is not in the noise on the dark current (which cannot be predicted), but in the absolute value (which can be estimated). The sample values for each pixel are used in the MDSI3 algorithm (see [RD5]), and this is not robust against biases in the inputs.

It is however relatively easy to estimate dark current accurately in orbit, and thus a dark current map was introduced in the simulator in order to assess the range error when such a map was used. The range error for the baseline sensor simulation with DC estimation is shown Figure 10:

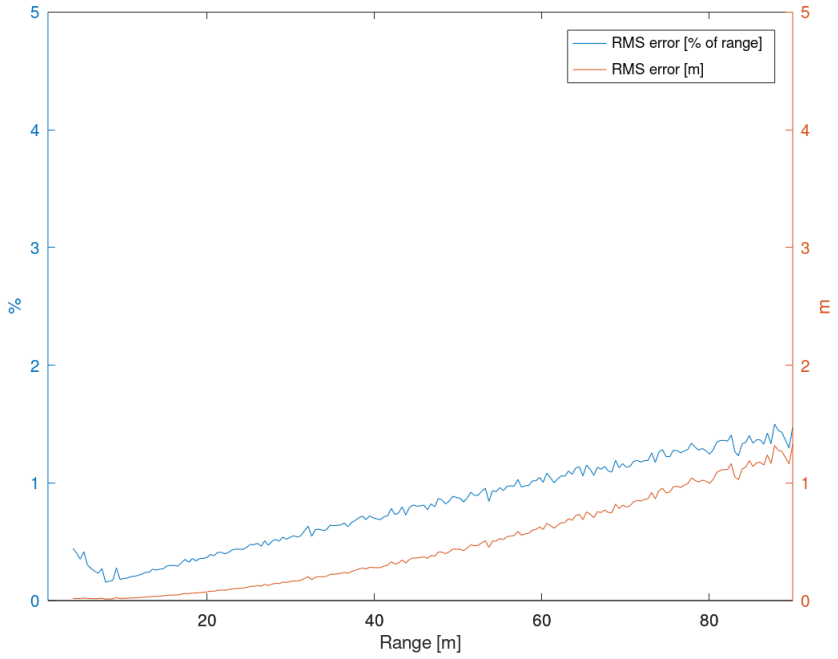

Figure 10: Baseline camera range performance EOL with DC estimation

By using an estimated DC map, the accuracy of the estimated range is thus increased by a factor of ~3, which is even better than the BOL accuracy without DC compensation.

The average bias (i.e. the average difference between actual and measured range) for the range simulations is shown in Figure 11:

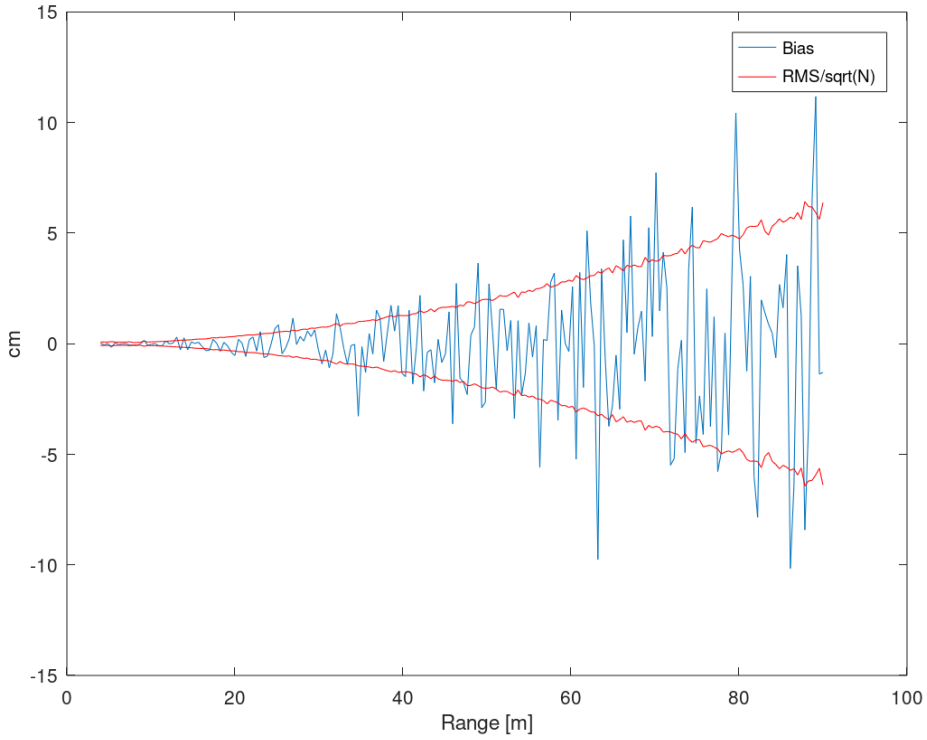

Figure 11: Baseline camera range bias

The average bias closely follows the RMS range error, as explicit biases (only dark current) simulated in the system are differenced out using the DC map estimation.

The number of accumulations used in the above simulations are shown in Figure 12 along with the maximum theoretical obtainable framerate.

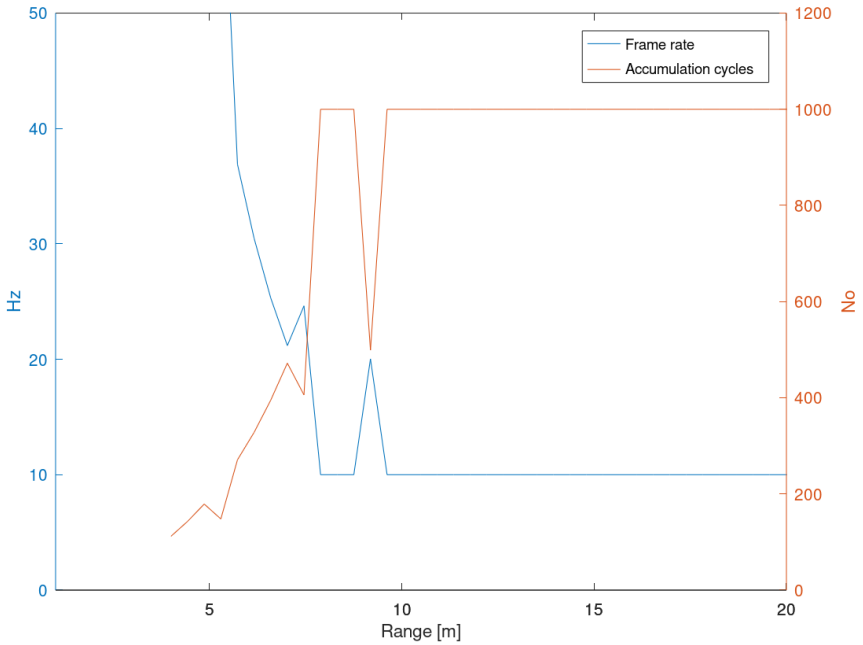

Figure 12: Accumulation cycles and associated frame rate obtained dynamically during simulations

The jerks in the curve is due to the (simulated) controller trying to decrease the accumulation cycles by 50% whenever full well capacity is reached. This happens at different times on different simulations due to noise.

11 Conclusion and Recommendations for EM Activities

The radiation tests performed during this study confirmed the initial assumption that the dark current of the QVGA ToF sensor would increase, and that SELs would probably occur. The SEL sensitivity is on par with e.g. the LCMS sensor – which is currently flight proven – indicating that this sensor can in fact be used as is on at least some specific space missions. A latch up protection circuit monitoring the voltage lines to the sensor is however required.

The performance analysis shows that even though the BOL dark current results were slightly worse than the initial assumptions during breadboard design, the sensor seems to perform very well, and even better than the breadboard ToF sensor, mostly due to higher FFxQE, lesser number of sub-pixels, and higher full-well capacity. The decrease in number of sub-pixels however does come at a price: The sensitivity to background light (direct sunlight and specular reflected sunlight) is inherently higher for this sensor, since there is no analog way to “empty” the sub-pixels, which may limit its use on specific missions. It should be noted, that in some cases it is still possible to do this digitally for high frame-rates and even background illumination. Terma believe that this is a suitable trade-off, given the better performance of the sensor.

Based on the test results as well as the conclusions from the previous ToF activities, the QVGA ToF sensor seems a viable candidate for a future space-borne 3D camera.

Terma’s recommendation for potential future EM activities goes as follows[2]:

1. We do propose to use COTS components whenever possible, but with the option of using rad-hard components for selected components.
2. *Sensor Breadboard*
   During the previous breadboard development, most of the sensor electronics were developed by TriDiCam, and the main interface was a bit pattern file for the FPGA to interpret. Apart from this there was not much visibility towards the sensor parameters and control strategy. Consequently, we propose to start out by establishing a flexible breadboard for performing test. Fraunhofer IMS already has the capability to readout sensor data, so a simple solution could be to augment the already existing test equipment for easy interface. Alternatively – if a fully standalone breadboard is needed – the readout electronics can be developed based on the Fraunhofer IMS reference design.
3. *Optical EM*
   An off-the-shelf laser driver was used during initial breadboard development. A flight-model design was however proposed, and components selected for this design. Since only one PLD was used during the initial breadboard design, we recommend to establish an EM of the optics module, including the 10+ PLDs and drivers necessary as well as the needed optics for each PLD.
4. *Power Supply Unit*
   The power supply unit should be able to handle all the (many) voltages to the QVGA ToF sensor as well as the high-current PLD drivers, while including a latch up protection and reset circuit. For the sensor breadboard and optical EM, this unit can in principle be omitted and substituted by lab supplies, but it would also be possible to build up a fully functional PSU EM in order to test noise on the sensor voltages as well as power and space constraints.
5. *Calibration Strategy*
   It became clear during the breadboarding activity that the calibration part of the sensor development was underestimated. A number of ground as well as in-orbit

[22] Note that some of these activities can be separate from the others.

calibration methodologies were proposed, and these need to be an integral part of the EM activities, as experience shows, that the performance of the sensor is heavily linked to a correct calibration. At the very least, these activities should cover ground calibration (initial DC map, measurement of timing parameters with respect to temperature, inter-pixel calibration, inter-PLD calibration etc.), as well as in-orbit calibration (integrated optical feedback loops, DC change assessments, ageing assessment etc.)

6. *Raw Data Processing*
   Although any data processing of ToF measurements starts with some form of the MDSI3 algorithm, this needs – for operational use – to be augmented with a number of algorithmic steps, remaining to be implemented. Special attention should be given to the following:
   a. Use of dark current estimates (see also calibration above) and associated temperature
   b. Use of inter-pixel timing variance calibration metrics (see also calibration above)
   c. Use of PLD/driver timing variance calibration metrics (see also calibration above) and associated temperature
   d. Use of ToF initial estimates to improve depth-of-field and obtain super-resolution. In order to increase robustness, the proposed ToF camera contains no moving parts and thus have a limited depth-of-field. However, as the ToF estimates gives very accurate estimates of the actual distance to the imaged objects, it is possible to re-compute the 3D point-cloud – taking into account the accurate representation of the optical properties of the camera – in order to improve the depth-of-field significantly as well as obtaining super-resolution of images.

The same technique can be used to detect and – to some degree – correct for the observed behavior at high-intensity horizontal variations, where the simple MDSI3 fails.

Fraunhofer-IMS has currently no plans for developing a VGA version of the sensor, however the results of this study might change this position.